Materials and Design 140 (2018) 307–316

Contents lists available at ScienceDirect

Materials and Design

journal homepage: www.elsevier.com/locate/matdes

Effect of scanning strategy on texture formation in Ni-25 at.%Mo alloys fabricated by selective laser melting

Shi-Hai Sun [a,b], Koji Hagihara [b,c], Takayoshi Nakano [a,b,*]

[a] Division of Materials and Manufacturing Science, Graduate School of Engineering, Osaka University, 2-1 Yamadaoka, Suita 565-0871, Japan
[b] Anisotropic Design & Additive Manufacturing Research Center, Osaka University, 2-1 Yamadaoka, Suita 565-0871, Japan
[c] Department of Adaptive Machine systems, Graduate School of Engineering, Osaka University, 2-1 Yamadaoka, Suita, Osaka 565-0871, Japan

HIGHLIGHTS

- Fabrication of Ni-25 at.%Mo product was succeeded by the selective laser melting.
- Texture development can be controlled by changing the scanning strategy of the laser.
- Aligned crystal orientation along the build direction can be varied in ⟨001⟩ or ⟨101⟩.
- Controlling mechanism of the texture was clarified by microstructure observation.

GRAPHICAL ABSTRACT

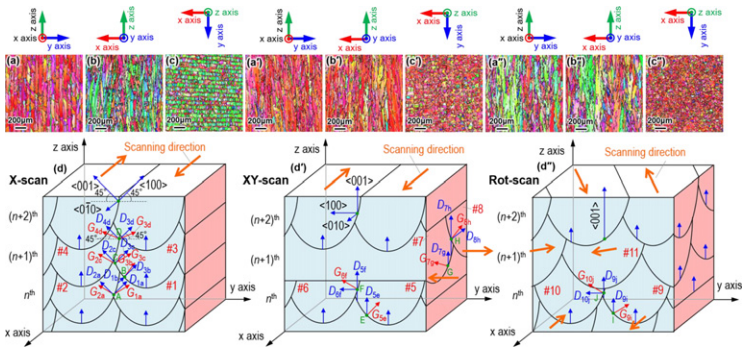

ARTICLE INFO

Article history:
Received 25 September 2017
Received in revised form 4 November 2017
Accepted 26 November 2017
Available online 28 November 2017

Keywords:
Additive manufacturing
Selective laser melting
Texture
Electron backscattering diffraction
Ni-Mo alloy
Short-range order

ABSTRACT

Variations in the crystallographic texture in Ni-25 at.%Mo alloys fabricated by selective laser melting with different scanning strategies were designed for the first time. Single-crystalline-like texture with a short-range order of Mo atoms can be produced via bidirectional scanning along one axis (X-scan) and bidirectional scanning with a 90° rotation in each layer (XY-scan), while only fiber texture was formed in bidirectional scanning with a 67° rotation (Rot-scan). The aligned crystal orientation along the build direction can be varied by the scanning strategy; ⟨001⟩ is preferred in the XY- and Rot-scan samples, while ⟨101⟩ is preferred in the X-scan sample. The controlling mechanisms of the texture, focusing on the preferential growth directions of the columnar cells and the following epitaxial growth, are discussed.

1. Introduction

Ni—Mo alloys have been used as coating, cathode, and catalyst materials because of their high strength, good corrosion and wear resistance, and high thermal stability [1–4]. However, it is reported that the corrosion resistance and ductility is deteriorated by discontinuous long-range ordering (LRO) to form Ni_4Mo or Ni_3Mo precipitates at the grain boundary [4–6]. Thus, a single crystalline microstructure is suggested as a means to reduce the precipitate at the grain boundaries. In addition, the single crystalline microstructure is preferred for applications at elevated temperatures in order to improve creep resistance. Therefore, it is necessary to establish a strategy to control

* Corresponding author at: Division of Materials and Manufacturing Science, Graduate School of Engineering, Osaka University, 2-1 Yamadaoka, Suita 565-0871, Japan.
E-mail address: nakano@mat.eng.osaka-u.ac.jp (T. Nakano).

https://doi.org/10.1016/j.matdes.2017.11.060

the microstructure in Ni-based alloys to improve their mechanical properties and corrosion resistance. The prevailing manufacturing methods to obtain single crystalline microstructure or directional solidification microstructure, are the floating zone method [7,8], the Czochralski method [7,9], and the Bridgman method [7,9], which require stringent temperature control. Thus, they require high cost, and are limited in terms of accessible sizes and shapes of the product.

Recently, the additive manufacturing (AM) technology has been reported to fabricate complex-structured components at a low cost in a short time [10–12]. The control of the microstructure and texture in samples built by AM have been reported in nickel-based alloys [13–18], cobalt-based alloys [19,20], titanium alloys [21–25], steels [26,27], aluminum alloys [28,29], and so on. In some reports, the formation of single-crystalline-like microstructures was presented [13–17,19,20,24,25]. In this study, we focused on the AM of Ni—Mo alloys, for which there have been no reports to date.

Although there are many reports on the development of textures in AM samples as described above, the controlling mechanisms of the textures have not been sufficiently clarified yet, as there are numerical influencing factors from the material and build parameter aspects, such as crystallographic structure, phase transformation, power, scanning speed, and scanning strategies. In Ni—Mo alloys, the development of short-range order (SRO) is known [4–6,30–33], whose developing feature is significantly varied depending on the cooling rate [4–6,30–33]. This is one of the reasons we focused on the Ni—Mo alloy for the AM process: not only for the practical aspect but also for the fundamental aspect; i.e., to clarify the controlling factors of the microstructure, including texture depending on the cooling rate by the observation of SRO. During this study, we found that the texture developed in the Ni—Mo alloy can be varied by the scanning strategy. The mechanism of this is discussed in this paper.

The development of the texture in the AM samples, and its variation in scanning strategy [13,14,21,25] has been reported by some researchers. Recently the formation mechanism of the texture in β-Ti with body-centered cubic (bcc) structure [25] was reported, but research in the face-centered cubic (fcc) phase is still not sufficient. Based on detailed observation of the microstructure, the developing mechanism of the texture, depending on the scanning strategy, in the fcc Ni—Mo alloy is discussed.

2. Experimental procedure

For the fabrication of the AM sample, gas-atomized powder with a nominal composition of Ni-25 at.%Mo was prepared, whose diameter ranged from 10 to 45 μm with an average of 34 μm. The other detectable element contents, in mass fraction, were 0.13% Fe, 0.1% Cu, 0.26% Si, 0.05% B, and 0.05% O. The powder exhibited a spherical shape with several satellites, as shown in Fig. 1. Using this powder, 10 mm × 10 mm × 5 mm blocks were built by selective laser melting (SLM) equipment (EOS M 290) under a power of 200 W, a scanning speed of 800 mm/s, and a pitch (i.e. the distance between neighboring scanning paths) of 0.08 mm with a layer thickness of 40 μm. In this study, the build direction was defined as the *z*-axis, and the scanning directions, which are perpendicular to the *z*-axis, were defined as the *x*- and *y*-axes. Three different scanning strategies, X-scan, XY-scan, and Rot-scan, were attempted to control the texture. In the X-scan, the laser beam was scanned bidirectionally along one axis (*x* only). In the XY-scan and Rot-scan, the bidirectional scanning was changed with a 90° rotation and 67° rotation in each layer, respectively. The samples were cut from stainless-steel platform by electric discharge machining directly, without performing any stress relieving treatment. The built samples were cut along the *xz*-, *yz*-, and *xy*-planes, and the microstructures were observed by scanning electron microscopy (SEM, JEOL JSM-6500F, Japan), and transmission electron microscopy (TEM, JEOL JEM-3010, Japan). All the microstructures of the samples were observed in the as-built state, without any heat treatment. Before the observation

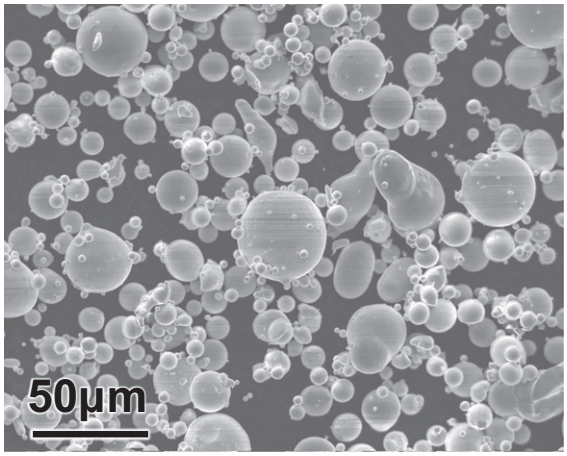

Fig. 1. Morphology of the powders used in the selective laser melting.

by SEM, the specimens were etched in a solution consisting of 31% HNO_3, 6% HCl, and 63% H_2O with ultrasonic vibration, to see the melt-pool trace and grain boundaries clearly. Textures developed in the samples were examined by electron backscatter diffraction (EBSD) pattern analysis in the SEM at the measured step size of 3 μm at low magnification and 0.5 μm at high magnification.

3. Results

The nearly full dense sample can be obtained in all the scanning strategies in the fabrication conditions described herein. The relative densities measured by the Archimedes method for the X-scan, XY-scan, and Rot-scan sample were 99.6%, 99.8%, and 99.8%, respectively. Fig. 2(a–i) shows the crystal orientation maps analyzed by SEM-EBSD on the *yz*-, *xz*-, and *xy*-planes of three samples built by the scanning strategies of X-scan, XY-scan and Rot-scan, respectively. In addition, the corresponding {001}, {101}, and {111} pole figures along the *z*-axis taken from the *xy*-plane of the samples are displayed in Fig. 2(j, k, l). Interestingly, it was found that the crystallographic textures developed in the different scanning strategies were wholly different from one another. In the XY-scan sample, strong ⟨001⟩ alignments occurred in *x*-, *y*-scanning and build directions (Fig. 2(b, e, h)). The corresponding {001} pole figure in Fig. 2(k) shows distinctly strong and sharp intensity peaks along the *x*-, *y*-, and *z*-axes, suggesting that a single-crystalline-like cube texture was developed. In the X-scan sample, there were the same ⟨001⟩ alignments along the *x*-scanning direction (Fig. 2(a)) as those in the XY-scan sample, but the preferred crystal orientation along the *y*-scanning and build directions were shifted from ⟨001⟩ to ⟨101⟩ (Fig. 2(d, g)). That is, a similar single-crystalline-like cube texture, but it is rotated along the *x*-scanning direction by 45° with respect to the one formed in the XY-scan, was developed in the X-scan. In addition, the intensity concentration of the orientations was somewhat broader in the X-scan than observed in the XY-scan sample, as shown in Fig. 2(j, k). This is because as well as the stronger concentration of ⟨101⟩ intensity, a weak concentration of ⟨001⟩ intensity was accompanied along the *z*-direction, as shown in Fig. 2(j). Such coexistence of concentrations of different orientations was not observed in the XY-scan sample. In the Rot-scan sample, on the other hand, a strong ⟨001⟩ alignment was developed only along the build direction (Fig. 2(c, f, i)). The {001} pole figure of Fig. 2(l) shows that a ring-like distribution of the ⟨100⟩ intensity with respect to the *z*-axis was developed in addition to the strong peak along the *z*-axis. This demonstrates that the ⟨001⟩ fiber texture was developed in the Rot-scan sample.

To clarify the origin for this variation in texture in different scanning strategies, detailed microstructural observations were conducted. Fig. 3(a) shows the TEM bright field image of the microstructure in the sample built by the XY-scan, and Fig. 3(b) shows the corresponding selected

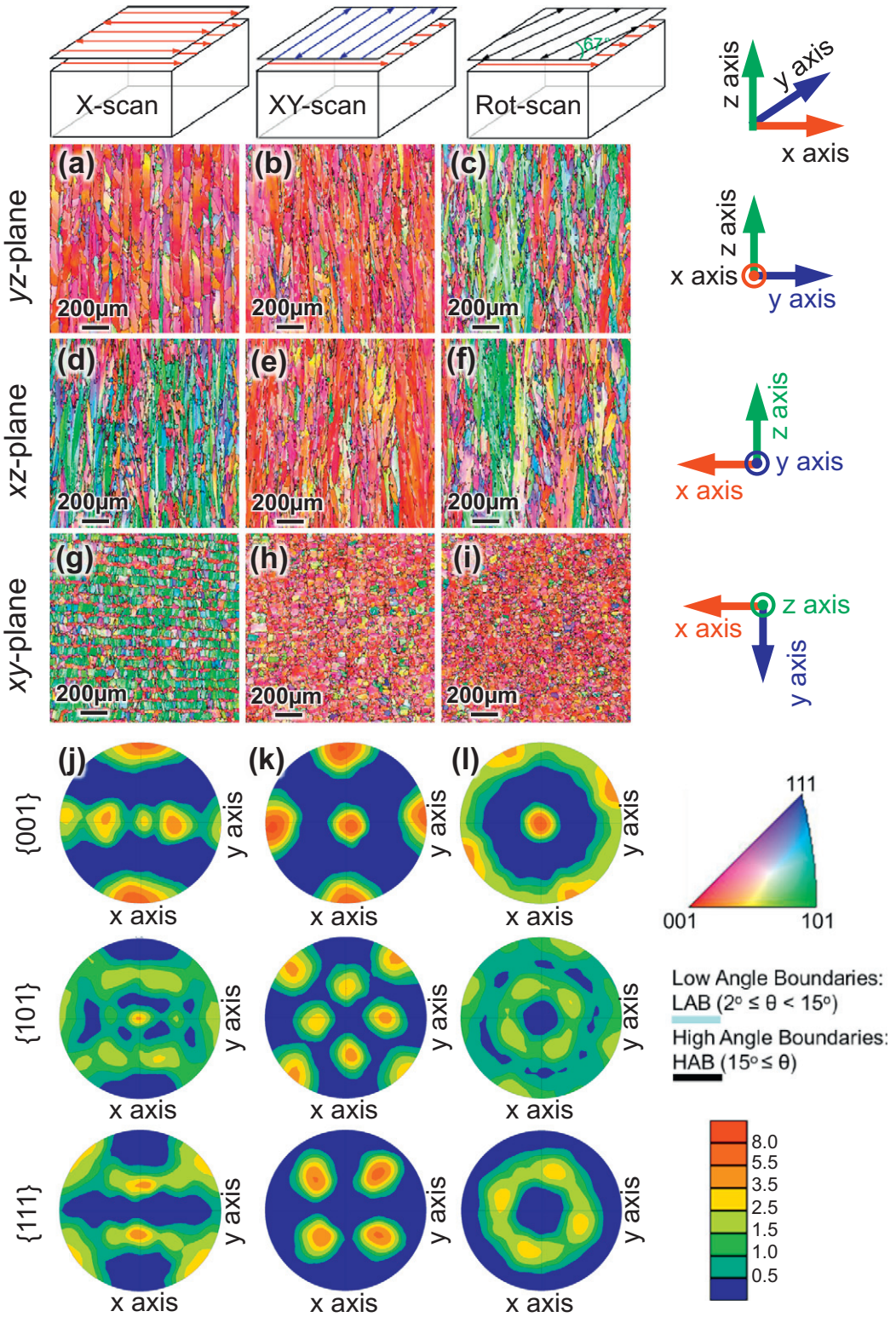

Fig. 2. Crystal orientation maps showing the variation in textures with scanning strategies of (a, d, g, j) X-scan, (b, e, h, k) XY-scan, and (c, f, i, l) Rot-scan in SLM of Ni-25 at.%Mo alloy, analyzed by SEM-EBSD. The crystal orientations expressed on the observation plane all correspond to the normal plane. (j, k, l) Corresponding {001}, {101}, and {111} pole figures along the *z*-axis, measured on the *xy*-plane.

area electron diffraction (SAED) pattern. Fig. 3(a) demonstrates that a cellular-like microstructure was developed in the solidification process of SLM. From the SAED pattern, the growth of the columnar cells can be found to preferentially occur in the 〈001〉 orientation, similarly to those observed in other fcc materials [34]. The observation was also conducted for the other two samples built by the X-scan and Rot-scan, and the same feature was confirmed. Note that there exist diffuse diffraction intensity profiles at the {0 1 1/2} positions beside those from the fcc matrix, as indicated by green circles in Fig. 3(b), indicating the development of SRO [4,30–33]. Regarding the detailed origin of the diffuse intensity maxima by SRO, Hata et al. [32,33] clarified in their high-resolution TEM observations and simulations that these were derived

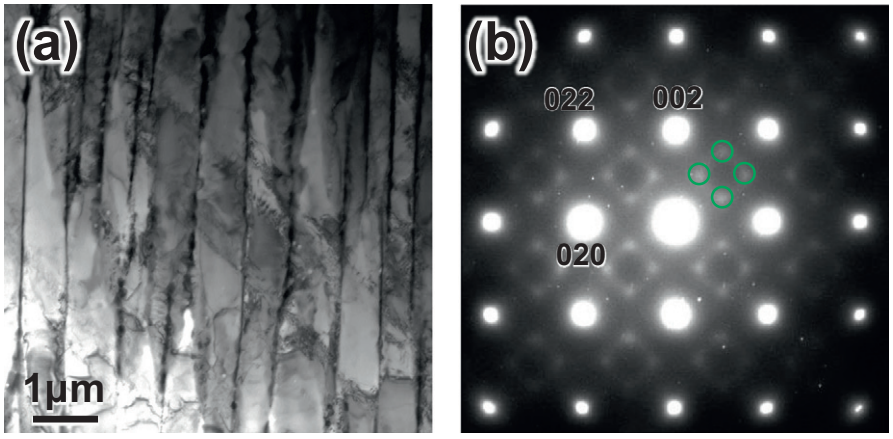

Fig. 3. (a) TEM bright field image of the microstructure and (b) corresponding SAED pattern observed in the Ni-25 at.%Mo sample fabricated in the XY-scan. The observed plane was nearly parallel to the *yz*-plane, and the specimen was slightly tilted to adjust the observed direction parallel to 〈100〉.

from the formation of microclusters of subunit cells of $D1_a$, $D0_{22}$, and Pt_2Mo structures. In addition, it was reported that the diffuse intensity maxima changed to sharp ordered spots, which are derived from stable ordered structures such as $D1_a$ (Ni_4Mo) and Pt_2Mo(Ni_2Mo)-type structures by further annealing, i.e., the LRO proceeds by long-term annealing at high temperature [4,30–33]. The developing LRO structure

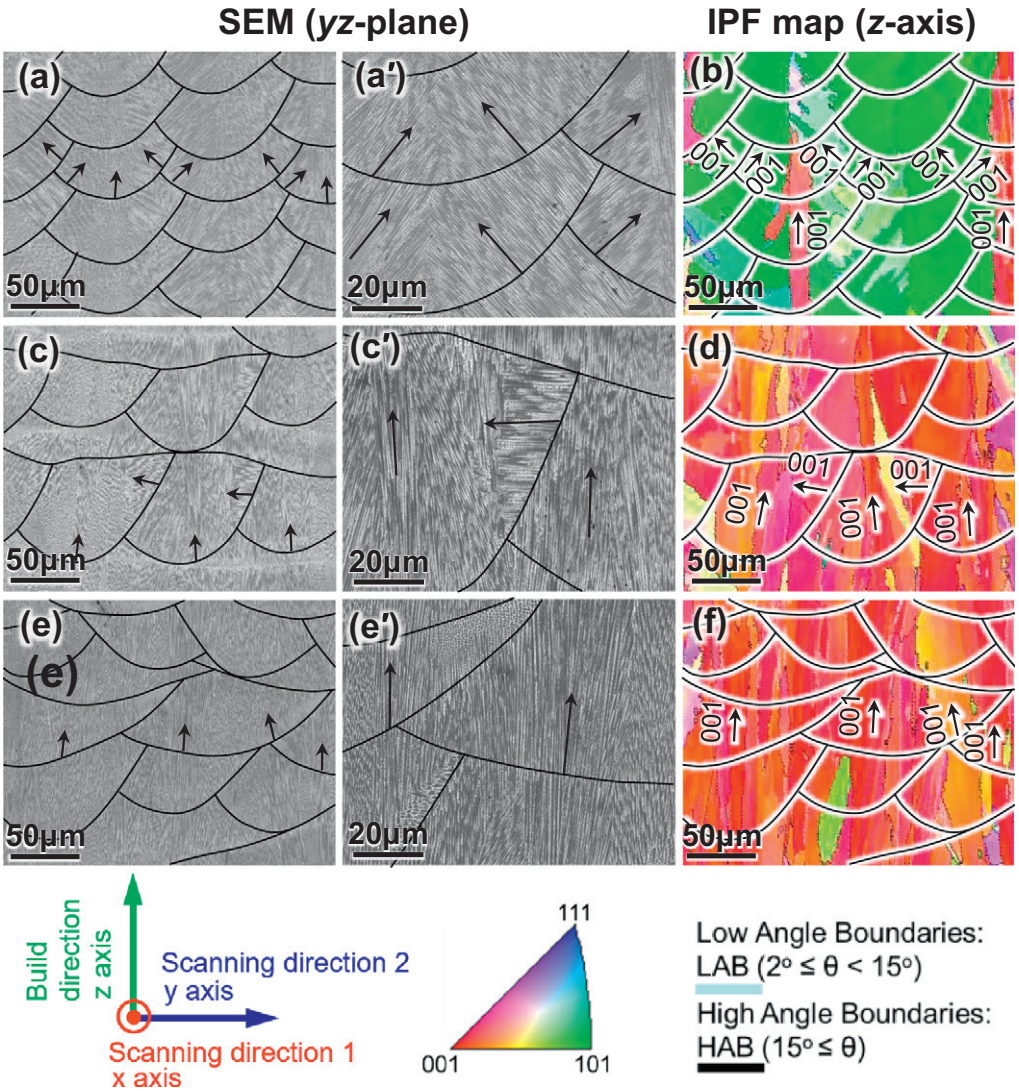

Fig. 4. (a, c, e) SEM image showing the morphologies of the boundaries of the columnar cells and the traces of the melt-pools observed on the *yz*-plane, and (b, d, f) corresponding crystal orientation maps along the z-axis analyzed by SEM-EBSD, in the samples fabricated by the scanning strategy of (a, b) X-scan, (c, d) XY-scan, and (e, f) Rot-scan. Figs. (a′, c′, e′) are the higher magnification images in Figs. (a, c, e), respectively. The black arrows indicate the elongation direction of the columnar cells observed on the cross-sections.

varies depending on the alloy composition and heat-treatment temperature [4,30–33].

The present TEM observation results suggest that the ordering transformation from SRO to LRO did not occur during the fabrication process, demonstrating the cooling rate in the AM sample fabricated under the present conditions is rather fast. This must be because of the short exposure time at high temperatures for the small build height in this study. In addition, the preheating temperature in the present SLM was only 80 °C, which is much lower than that in electron-beam melting (EBM). Because the preheating temperature in EBM is approximate 0.5–0.8 of the melting point of the material, the microstructure of the early-built part can be affect greatly [20]. Now, the study to clarify the relation between the specimen shape, fabrication condition, etc. and the cooling rate, and resultant variation in texture is ongoing, by more quantitative analysis of the difference in the morphology and intensity of the SRO. The result on this will be described in a separated paper.

Fig. 4(a, c, e) displays the SEM images on the *yz*-plane showing the morphologies of the boundaries of the columnar cells and the traces of melt-pools enhanced by etching in the samples built by different scanning strategies. In addition, enlarged SEM images are shown in Fig. 4(a′, c′, e′). Fig. 4(b, d, f) shows the corresponding crystal orientation maps at the same positions shown in Fig. 4(a, c, e). Note that although the observed direction of the microstructures in Fig. 4 is parallel to *x*-axis, the crystal orientations expressed are all corresponding to the one along the *z*-axis (build direction) in Fig. 4(b, d, f). The layered half ellipses accumulated along the *z*-axis in Fig. 4(a, c, e) were identified as melt-pool traces, but the detailed morphologies were largely different in each sample due to the different scanning strategies used. When viewed along the *x*-direction, the melt-pool traces with half-ellipse shapes were periodically arranged in the X-scan sample, while the arrangement is somewhat irregular, and the shape of melt-pool is flatter in the Rot-scan sample. In the XY-scan sample, in addition to the half-ellipse shape of the melt-pool traces, band-like morphologies were observed which stem from the melt-pools formed by the scan along the *y*-direction.

In addition to the difference in the shapes of the melt-pools, the extending directions (indicated by black arrows) of the columnar cells in the melt-pool were found to be different. In the X-scan sample, most of the columnar cells in the melt-pool were inclined approximately 45° toward the center, and only a few columnar cells at the central position grew along the build direction. As demonstrated in Fig. 3, the extending directions of the columnar cells are parallel to ⟨001⟩.

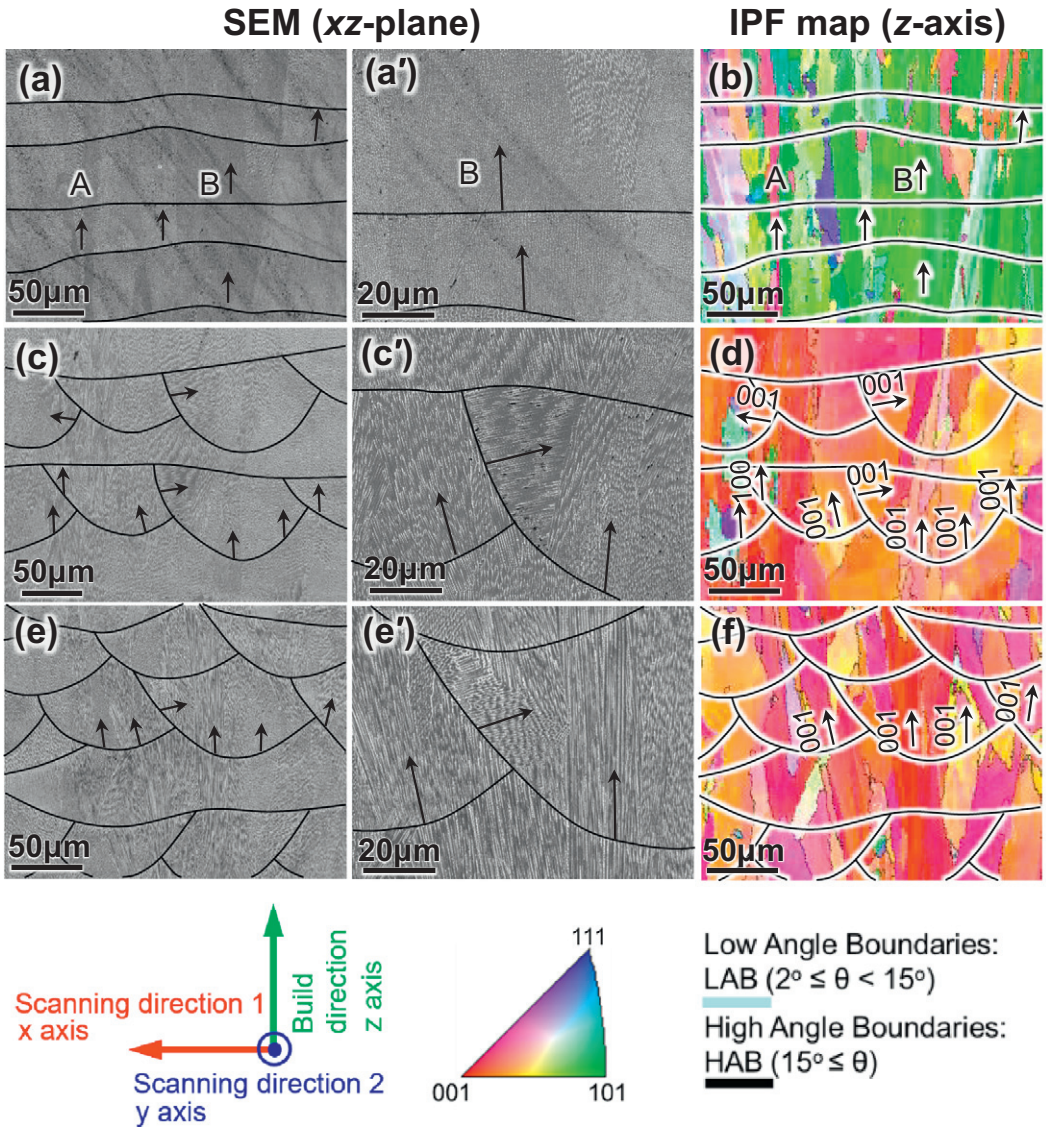

Fig. 5. (a, c, e) SEM image showing the morphologies of the boundaries of the columnar cells and the traces of melt-pools observed on the *xz*-plane, and (b, d, f) corresponding crystal orientation maps along the *z*-axis, analyzed by SEM-EBSD, in the samples fabricated by the scanning strategy of (a, b) X-scan, (c, d) XY-scan, and (e, f) Rot-scan. Figs. (a′, c′, e′) are the higher magnification images of Figs. (a, c, e), respectively.

Thus, the comparison of the microstructure and the crystal orientation map shown in Fig. 4(a, b) demonstrates that the 45°-inclined columnar cells and the vertical columnar cells at the central position of the melt-pools become the origin of the development of the strong ⟨101⟩ texture and weak ⟨001⟩ texture along the build direction, respectively.

However, in the XY-scan and Rot-scan samples, many of the columnar cells tended to grow along the build direction, and elongated grains were developed beyond the melt-pool boundaries, as shown in Fig. 4(c, e). Comparing the microstructure and the crystal orientation map shown in Fig. 4(c, e) and (d, f), respectively, it can be found that these elongated grains aligned along the build direction contribute to the development of the ⟨001⟩ texture. Note that in the XY-scan sample, the elongated grains along the build direction located in the overlapping regions of the half-ellipse shapes of the melt-pools partly consist of columnar cells grown along the horizontal direction, beside the vertically grown columnar cells, as shown in Fig. 4(c, c′).

To further understand the 3D grain and columnar cell arrangement in the melt-pools and their effect on the texture development, Figs. 5 and 6 show the SEM images and their corresponding crystal orientation maps at the same positions observed on the *xz*- and *xy*-planes of the samples built by different scanning strategies, respectively. In Fig. 5(b, d, f), although the observed direction of the microstructures is parallel to the *y*-axis, the crystal orientations expressed all correspond to the one along the *z*-axis (build direction), as well as that in Fig. 4. When viewed along the *y*-direction, different from those observed in *x*-direction, only band-like morphologies were seen in the SEM image of the X-scan sample (Fig. 5(a)), which stem from the melt-pools formed by the scan along the *x*-direction. The extending directions (indicated by black arrows) of the columnar cells in Fig. 5(a, a′) were perpendicular to the horizontal melt-pool traces, which suggests that the growth of the columnar cell mainly occurs on the plane perpendicular to the *x*-scanning direction. As the columnar cells extended along ⟨001⟩, Fig. 5(b) suggests that the columnar cells with red color, at position A, extend along the build direction, and the columnar cells with green color, at position B, incline approximately 45° from the build direction on the *yz*-plane. In the SEM images of the XY-scan and Rot-scan samples (Fig. 5(c, c′, e, e′)), a similar melt-pool trace morphology and growth behavior of the columnar cells to those observed on the *yz*-planes (Fig. 4) can be seen. Periodic half-ellipse and band-like melt-pool traces were observed in the XY-scan sample; the columnar cells mainly extended vertically at the central region, and some columnar cells extended horizontally at the side regions of the melt-pools, as shown by the black

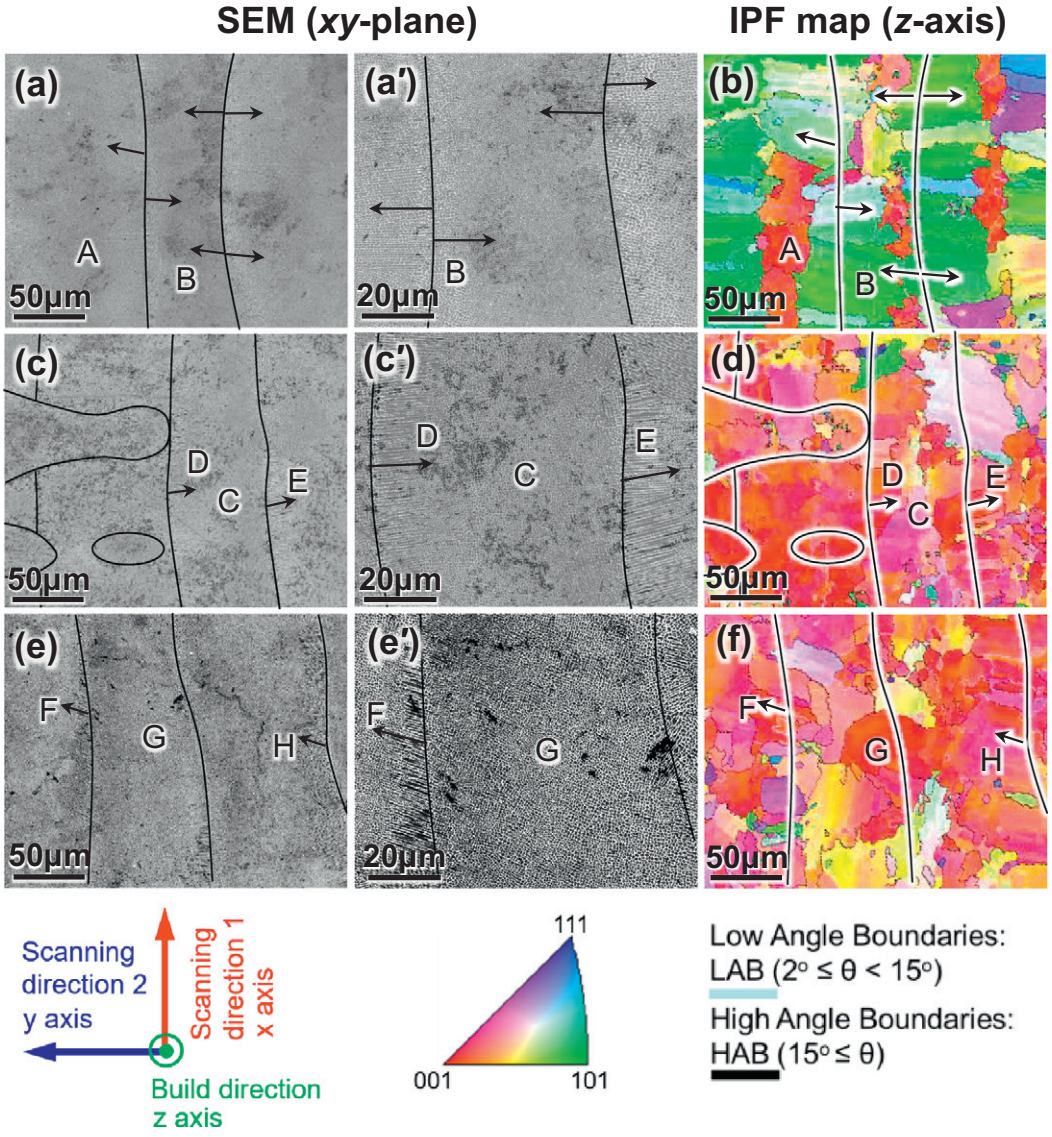

Fig. 6. (a, c, e) SEM image showing the morphologies of the boundaries of the columnar cells and the traces of melt-pool observed on the *xy*-plane, and (b, d, f) corresponding crystal orientation maps along the *z*-axis analyzed by SEM-EBSD, in the samples fabricated by the scanning strategy of (a, b) X-scan, (c, d) XY-scan, and (e, f) Rot-scan. Figs. (a′, c′, e′) are the higher magnification images of Figs. (a, c, e), respectively.

arrows. These vertically and horizontally extended columnar cells formed the ⟨001⟩ texture in the build direction, as shown in the corresponding crystal orientation map in Fig. 5(d). Irregular half-ellipse melt-pool traces were observed in the Rot-scan sample. Many of the columnar cells extended vertically in the melt-pools and elongated grains developed beyond the melt-pool boundaries. They formed the ⟨001⟩ texture in the build direction, as shown in Fig. 5(f).

When viewed along the *z*-direction, all the samples show band-like morphologies, which are thought to be from the melt-pool traces parallel to the scanning direction, as shown in Fig. 6. Moreover, in the XY-scan sample, besides the band-like morphologies, some rod-like and elliptical shapes, whose elongated directions were perpendicular to those of the main band-like morphologies, can also be observed. They are thought to arise from the part of the melt-pool traces in the layer above the main band-like morphologies' existing layer, which are not wiped off completely during the polishing process because of their greater depth caused by fluctuations in the melt-pool size. In the X-scan sample, the red grains, such as the one at position A, were in the center of the melt-pool trace, while the green grains, such as the one at position B, occupied a part of each of the neighboring melt-pool traces, as shown in Fig. 6(b). This kind of orientation distribution is consistent with the observation result on the *yz*-plane in Fig. 4(b). The extending directions (indicated by black arrows) of the columnar cells shown in Fig. 6(a, a′) were nearly perpendicular to the elongated direction of the melt-pool trace, i.e., the scanning direction. This further suggests that the grains mainly grow on the plane perpendicular to the scanning direction. As the columnar cells extended along ⟨001⟩, the crystal orientation in Fig. 6(b) suggests that the columnar cells at position A of Fig. 6(a) extend along the build direction, while those at position B incline approximately 45° from the build direction on the *yz*-plane.

For the XY-scan and Rot-scan samples, although the grains displayed a similar orientation in the build direction, as shown in Fig. 6(d, f), some different morphologies of microstructure were observed depending on the position. That is, at the central position of the melt-pools, such as positions C and G, the columnar cells whose lengths of the boundaries are short were observed, i.e. they were aligned parallel to the build direction in the center of the melt-pool traces. While columnar cells whose lengths of the boundaries are long were aligned nearly along the direction perpendicular to the scanning direction (black arrows) on the side of the melt-pool traces, such as at positions D, E, F, and H, as shown in Fig. 6(c, c′, e, e′). These observations further support the conclusion that the growth of columnar cells mainly occurs on the plane perpendicular to the scanning direction in all the samples in which strong textures were developed, independent of the scanning strategy.

4. Discussion

It is generally known that the growth preference of the columnar cells is along the direction with the largest temperature gradient. In the melt-pool, the largest temperature gradient direction lies along the direction perpendicular to the melt-pool boundary [21]. Thus, in the ideal condition where the crystal growth occurs only by the effect of the thermal gradient, the columnar cells would grow along a radial direction in the melt-pool. This is obviously different from the observation results shown in Figs. 4–6. This suggests that other factors also contribute to the growth behavior of the columnar cells, which induce the formation of peculiar textures varied by the scanning strategy.

Here, it must be emphasized, as the important observation result found in this study, that the growth of the columnar cells preferentially occurred within the plane perpendicular to the scanning direction in the textured samples. This implies that the ⟨001⟩ growth direction lies on the plane perpendicular to the scanning direction in the strongly textured samples. Focusing on these features, the formation mechanism of the texture, which varied depending on the scanning strategy, is discussed in this section.

Fig. 7(a–c) shows schematic images, which explain the texture formation process in the X-scan, XY-scan, and Rot-scan, respectively. In the images, the melt-pools are numbered as #*i*, where $i = 1, 2, 3\ldots$, which are formed in the order of the numbers. The temperature gradient at the different solidification interface of the #*i* melt-pool is designated as G_{ik}, indicated by the red arrow, where *k* is the position A, B…, denoted by the corresponding lower-case letter. The extending

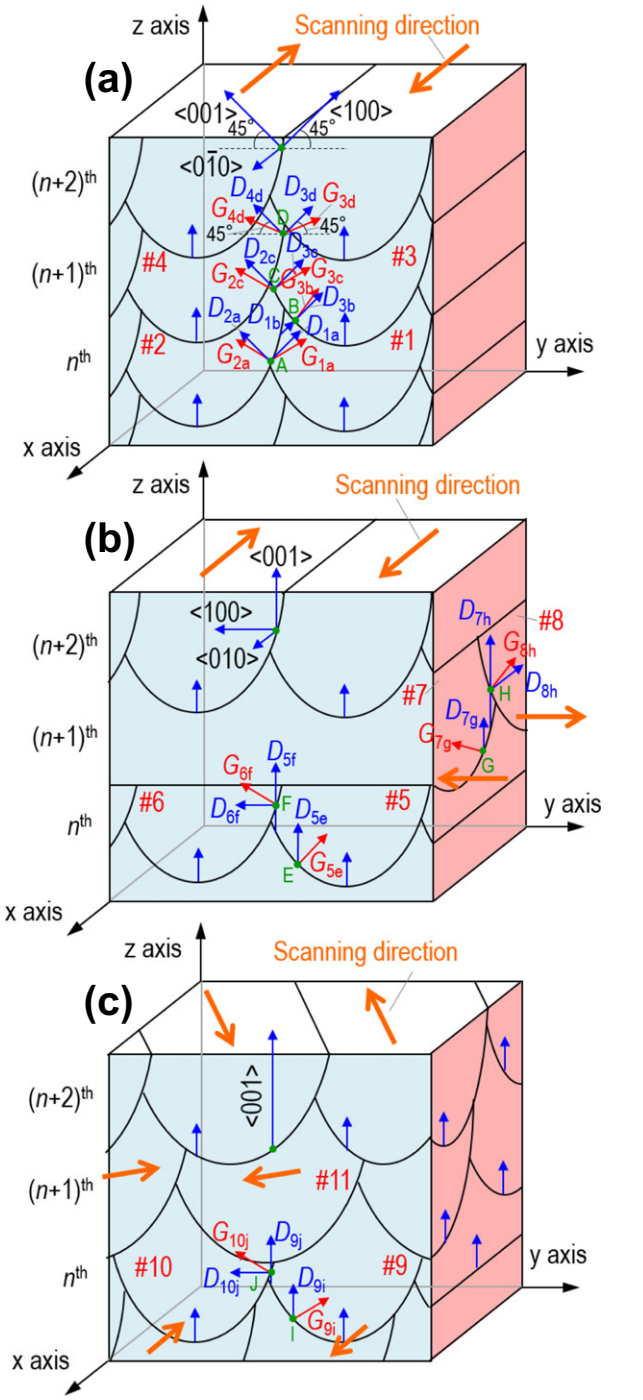

Fig. 7. Schematic drawings depicting the formation mechanisms of different microstructures and textures depending on the scanning strategy of the Ni-25 at.%Mo alloy. (a) X-scan, (b) XY-scan, and (c) Rot-scan. The red and blue arrows indicate the thermal gradient direction and expected ⟨001⟩ directions of the columnar cells, i.e., preferential growth direction of the columnar cells, respectively.

direction of the columnar cells is designated as D_{jk}, $j = 1, 2, 3\ldots$, indicated by the blue arrow, and the columnar cells extending along the D_{jk} direction are called the D_{jk} cells.

First, we focus on the growth behavior of columnar cells in the X-scan sample, as shown in Fig. 7(a). In the central position of the melt-pools, the temperature gradient directions are parallel to the build direction, so a few columnar cells grow vertically along the temperature gradient direction. They can go through several layers, because the extending direction controlled by the temperature gradient always matches the growth direction of the columnar cells beneath the melt-pool, and thus the epitaxial growth is assisted. As clarified in Fig. 3, the extending direction of the columnar cells is parallel to ⟨001⟩ in this Ni—Mo crystal. Thus, the development of these vertically grown columnar cells induces a weak ⟨001⟩ alignment of the crystal orientation, as confirmed in Fig. 2(j). At the boundary of the neighboring melt-pools, on the other hand, growth of the columnar cells occurred along the direction largely inclined from the build direction. Focusing on the growth behavior in this region, for example at position A, where the #2 melt-pool overlaid the #1 melt-pool, the columnar cells in the #2 melt-pool prefer to grow along the D_{2a} direction, which is perpendicular to the D_{1a} direction, rather than growing along G_{2a}, as was frequently observed in Fig. 4(a, a′). This D_{2a} direction corresponds to the secondary growth direction of the D_{1a} cell. It was observed in this study (Figs. 4–6) that the growth of columnar cells mainly occurs on the plane perpendicular to the scanning direction in all the samples in which strong texture was developed by the appropriate control of the AM process conditions. The texture development in the X-scan sample can be explained by the fact that the secondary growth direction of the cell, which is perpendicular to the primary extending direction of the columnar cell and lies on the plane perpendicular to the scanning direction, also becomes parallel to ⟨001⟩, as well as the primary extending direction of the cell. Under this situation, it can be understood that the growth along the D_{2a} direction occurs due to the decrease in nucleation energy by conserving the crystal orientation between the #1 and #2 melt-pools. Here, the smaller the angle between D_{2a} and G_{2a}, the easier the epitaxial growth, and thus changing frequency of the cell growth direction from G_{2a} to D_{2a} will increase. This can be conserved under the appropriate AM process conditions for the development of strong texture. That is, under the appropriate process conditions in the present study, D_{1a} and G_{2a} can both reside on the *yz*-plane as shown in Figs. 4 and 5. In this case, the ⟨010⟩ secondary growth direction of the D_{1a} cell at position A, which is on the same *yz*-plane, will have the smallest angle with G_{2a} compared to the ⟨010⟩ secondary growth direction of D_{1a} cells not on the *yz*-plane. Thus, this small deviation angle effectively assists the epitaxial growth of the columnar cells, whose ⟨010⟩ secondary growth direction is on the plane perpendicular to the scanning direction.

Then, in the scanning of the $(n + 1)^{th}$ layer, for example when considering the growth behavior at position B, the growth direction of the columnar cells in the left half of the #3 melt-pool will match the columnar cells on the left half of the #1 melt-pool. That is, at position B, the D_{3b} cell tends to grow along the D_{1b} direction for epitaxial growth to decrease the nucleation energy, rather than grow along the G_{3b} direction as shown in Fig. 4(a, a′). In the same way, at positions C and D, similar to the epitaxial growth at position A, the D_{3c} and D_{4d} cells prefer to grow parallel to the secondary growth direction of the D_{2c} and D_{3d} cells, respectively. After the columnar cells grow as mentioned above in several layers, both the primary and secondary growth direction of the columnar cells in melt-pools will be fixed on the *yz*-plane, inducing ⟨100⟩ alignment along the *x*-scanning direction. Then, to minimize the mismatch angle in the system, the competition growth along the temperature gradient direction or the epitaxial direction will cause most of the columnar cells to incline at approximately 45° with respect to the build direction during the SLM process of several layers in the X-scan. The same incline angle was reported by Dinda et al. [13] in a study of the texture evolution of IN718 fabricated by direct metal laser deposition. Here, the extending directions of the columnar cells with a 45° incline angle with respect to the build direction are parallel to the ⟨001⟩ orientation. As a result, the preferential alignment of ⟨101⟩ orientation occurs along the build direction in the X-scan sample.

In the XY-scan sample, the growth of the columnar cells occurred parallel or perpendicular to the build direction, different from the case observed in the X-scan sample, as shown in Figs. 4 and 5. Although the texture formation in the XY-scan has been explained by several researchers [14–16,19–21,24,25], the details have not been sufficiently clarified. Here, the texture development in the track-by-track and layer-by-layer process is considered in the growth mechanism of the XY-scan sample shown in Fig. 7(b). In the central position of the melt-pools in the n^{th} layer, the columnar cells prefer to grow vertically under the control of the temperature gradient direction. In addition, even away from the central part of the melt-pools in the n^{th} layer, where they overlaid the underlying melt-pools, for example at position E of the #5 melt-pool, although the G_{5e} deviates from the build direction, the extension of the D_{5e} cell was preferred to be parallel to the build direction, as observed in Figs. 4 and 5. This is in good agreement with the report in the bcc-Ti alloy by Ishimoto et al. [25]. Different from the case observed in the X-scan sample, under the requirement to decrease the nucleation energy by conserving the crystal orientation between melt-pools in the neighboring layers in which the scanning direction was rotated 90°, the best solution to minimize the angle between the epitaxial growth direction of the underlying columnar cells (on the *xz*-plane) and the temperature gradient direction in the new growing layer (on the *yz*-plane) is obtained by the growth parallel to the build direction [25]. In addition, when focusing on the growth at the side boundary of the neighboring melt-pools, for example at position F, where the #6 melt-pool overlaid the #5 melt-pool, the growth of the columnar cells along the direction perpendicular to the build direction was also observed in the #6 melt-pool. The origin of the development of these horizontally extending columnar cells is similar to those at position A in the X-scan sample. As the growth mechanism of the columnar cells at position F in the melt-pool #6, the epitaxial growth from the secondary growth direction of the D_{5f} cell in the #5 melt-pool is expected to reduce the nucleation energy. Under this situation, D_{5f} cells with a ⟨010⟩ secondary growth direction on the *yz*-plane must be preferentially remained in the developing process of the microstructure, since such cells effectively assist the epitaxial growth of the columnar cells along the horizontal direction in the #6 melt pool (i.e. D_{6f} cells). These cells can have the smallest angle with G_{6f} with keeping the crystal orientation in the neighboring layers.

At the boundary of the melt-pools in the n^{th} and $(n + 1)^{th}$ layers, such as position G in the #7 melt pool, the D_{7g} cell prefers to grow vertically to show epitaxial growth with respect to the underlying cells, as described above. If the underlying cells are located at a position similar to F, the ⟨010⟩ secondary growth directions of the D_{7g} cell will be fixed to the *x*- and *y*-axes owing to the above-described reason. If the underlying cells are located near the central position of the melt-pool, like at position E, however, the ⟨010⟩ secondary growth directions of the D_{7g} cell will not be fixed. However, in this case, if the D_{7g} cell, in which its secondary growth direction is not on the *xz*-plane, is formed, it will not be preferred for epitaxial growth in the neighboring #8 melt-pool. Because the secondary growth direction of the columnar cell has a larger angle with the temperature gradient direction in the #8 melt-pool, and it will cease to grow in the following layer. At the boundary of the neighboring melt-pools in the $(n + 1)^{th}$ layer, for example at position H, where the #8 melt-pool overlaid the #7 melt-pool, as in the case at position F, the D_{8h} cell prefers to grow horizontally along the secondary growth direction of the D_{7h} cell, which is on the *xz*-plane, as observed in Figs. 4 and 5, to decrease the nucleation energy by conserving the crystal orientation in the neighboring melt-pools. After the growth of the columnar cells in the way described in several layers, the majority of the cells will grow vertically or horizontally, on the plane perpendicular to the scanning direction. As the extending directions of

the columnar cells are parallel to ⟨001⟩, the ⟨001⟩ alignment will be developed in the *x*-, *y*-, and *z*-axes, forming a cube texture.

Fig. 7(c) shows the growth mechanism of the Rot-scan sample. For convenience, the scanning direction is assumed to be parallel to the *x*-direction in the n^{th} layer of the Rot-scan sample. Because the scanning direction rotates by 67° every layer, the melt-pool centers in the neighboring layers do not coincide with each other, and the appearance of the melt-pools in the cross-section exhibits irregular half ellipses with different morphology in each layer, as observed in Figs. 4 and 5. Such mismatch of the positions of the melt pool in each layer must prevent the development of single-crystalline-like texture in the Rot-scan sample.

In the central position of the melt-pools in the n^{th} layer, the extension of the columnar cells is preferred to be parallel to the build direction under the control of the temperature gradient. At the side part of melt-pools in the n^{th} layer, where they overlaid the underlying melt-pools, for example at position I in the #9 melt-pool in Fig. 7(c), the growth along the thermal gradient direction G_{9i} is naturally preferred. In this case, however, both the primary growth direction and the secondary growth direction will not match those of the columnar cells formed in the #11 melt-pool in the $(n+1)^{th}$ layer. This means the nucleation of new cells must occur in the #11 melt-pools, which requires extra energy. The way to reduce the extra energy required for nucleation is the preferential growth of the columnar cells along the vertical direction over a wider area of the melt-pool. If such vertical growth occurs, the successive growth keeping the primary ⟨001⟩ growth direction can occur beyond the melt-pool boundaries in each layer, although complete epitaxial growth, where the secondary growth direction also matches that in the neighboring layers, as observed in the XY-scan sample, is difficult to achieve. Thus, only the crystal orientation in the build direction is fixed, while the crystal orientation in the scanning direction is random. This assumption is in good agreement with the observation result of the crystal orientation map shown in Fig. 8, examined along the *y*-direction. The crystal orientation map clearly demonstrates that most of the columnar cells in the melt-pool grew along the build direction and elongated grains developed across several layers, but the crystal orientation along the direction perpendicular to the build direction is different in each grain. As shown in Fig. 5(e, e′), only at the narrow side region of the melt-pool, columnar cells extended perpendicular to the building direction were observed. Their formation mechanism is considered to be the same as those observed in the XY-scan sample, i.e., the secondary growth direction is on the plane perpendicular to the scanning direction, as shown at position J. However, these columnar cells did not significantly develop since the secondary growth direction cannot be conserved in the next $(n+1)$ scan layer. This must be the reason why the ⟨001⟩-fiber texture, in which only one of three ⟨001⟩ orientations is aligned parallel to the build direction, was developed in the Rot-scan sample.

Overall, we found that texture control of the Ni—25Mo alloy is possible by the appropriate selection of scanning strategy. For the acquisition of quantitative data to support the qualitative analysis in this study, the simulation works etc. are on-going in our group. These results will be described elsewhere.

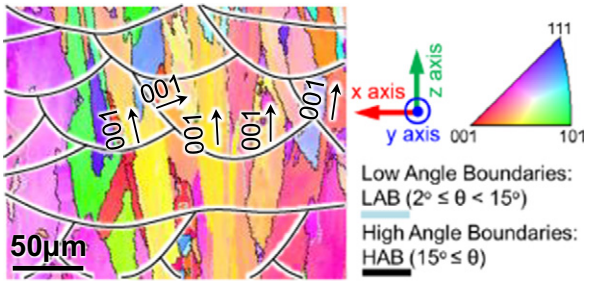

Fig. 8. Crystal orientation maps in the Rot-scan sample analyzed along the *y*-axis, at the position shown in Fig. 5(e).

5. Conclusions

We found that the control of texture in the Ni—Mo alloys can be accomplished by changing the scanning strategy with a suitable combination of power, pitch and scanning speed. This was achieved via the control of the selection of preferentially grown columnar cells at the initial stage, which can be varied depending on the scanning strategy, and following their epitaxial growth. It was found that the control of the sample fabricating conditions which induce the growth of the columnar cells within the plane perpendicular to the scanning direction, is important for the development of strong texture. Under this situation, the columnar cells in which not only preferential growth direction of ⟨001⟩, but also the ⟨010⟩ secondary growth direction lie on the plane perpendicular to the scanning direction, preferentially remain in the developing process of the microstructure in the X-scan and XY-scan samples, resulting in the development of single-crystalline texture. While such growth behavior of the columnar cells induces the development of a one-dimensional fiber-like texture in the Rot-scan sample.

These texture controlling methods must be applicable not only to the Ni—Mo alloy investigated in this study but also to other fcc and bcc materials in which the preferential growth direction of the columnar cells is parallel to ⟨001⟩. The epitaxial growth found for the development of the texture in this study is an indispensable factor that should be considered in the simulation of microstructure development in the AM process.

Acknowledgements

This work was supported by the Council for Science, Technology and Innovation (CSTI), the Cross-Ministerial Strategic Innovation Promotion Program (SIP), and Innovative Design/Manufacturing Technologies (Establishment and Validation of the Base for 3D Design & Additive Manufacturing Standing on the Concepts of Anisotropy & Customization) from the New Energy and Industrial Technology Development Organization (NEDO). This work was also supported by Grants-in-Aid for Scientific Research (S) from the Japan Society for the Promotion of Science (grant number 25220912).

References

[1] J.F. Kriz, H. Shimada, Y. Yoshimura, N. Matsubayashi, A. Nishijima, Nickel-containing catalysts for hydroprocessing of aromatic oils, Fuel 74 (1995) 1852–1857.
[2] P.C. Huang, K.H. Hou, G.L. Wang, M.L. Chen, J.R. Wang, Corrosion resistance of the Ni-Mo alloy coatings related to coating's electroplating parameters, Int. J. Electrochem. Sci. 10 (2015) 4972–4984.
[3] M. Manazoğlu, G. Hapçi, G. Orhan, Electrochemical deposition and characterization of Ni-Mo alloys as cathode for alkaline water electrolysis, J. Mater. Eng. Perform. 25 (2016) 130–137.
[4] H.M. Tawancy, Long-range ordering behaviour and mechanical properties of Ni-Mo-based alloys, J. Mater. Sci. 30 (1995) 522–537.
[5] B. Chakravarti, E.A. Starke, B.G. Lefevre, Order-induced strengthening in Ni_4Mo, J. Mater. Sci. 5 (1970) 394–406.
[6] H.M. Tawancy, F.K. Alyousef, Effect of long-range ordering in a Ni-Mo alloy on its mechanical properties and corrosion resistance, J. Mater. Sci. 42 (2007) 9121–9124.
[7] R.W.K. Honeycombe, The growth of metal single crystals, Metall. Rev. 4 (1959) 1–47.
[8] S. Asai, Recent development and prospect of electromagnetic processing of materials, Sci. Technol. Adv. Mater. 1 (2000) 191–200.
[9] U.Â.H. Fredriksson, Solidification and Crystallization Processing in Metals and Alloys, John Wiley & Sons, 2012.
[10] N. Guo, M.C. Liu, Additive manufacturing: technology, applications and research needs, Front. Mech. Eng. 8 (2013) 215–243.
[11] D. Herzog, V. Seyda, E. Wycisk, C. Emmelmann, Additive manufacturing of metals, Acta Mater. 117 (2016) 371–392.
[12] C. Köroner, Additive manufacturing of metallic components by selective electron beam melting-a review, Int. Mater. Rev. 61 (2016) 361–377.
[13] G.P. Dinda, A.K. Dasgupta, J. Mazumder, Texture control during laser deposition of nickel-based superalloy, Scr. Mater. 67 (2012) 503–506.
[14] F. Geiger, K. Kunze, T. Etter, Tailoring the texture of IN738LC processed by selective laser melting (SLM) by specific scanning strategies, Mater. Sci. Eng. A 661 (2016) 240–246.
[15] K. Kunze, T. Etter, J. Grässlin, V. Shklover, Texture, anisotropy in microstructure and mechanical properties of IN738LC alloy processed by selective laser melting (SLM), Mater. Sci. Eng. A 620 (2015) 213–222.

[16] H. Helmer, A. Bauereiß, R.F. Singer, C. Körner, Grain structure evolution in Inconel 718 during selective electron beam melting, Mater. Sci. Eng. A 668 (2016) 180–187.
[17] M. Ramsperger, R.F. Singer, C. Körner, Microstructure of the nickel-base superalloy CMSX-4 fabricated by selective electron beam melting, Metall. and Mat. Trans. A 47A (2016) 1469–1480.
[18] D.Q. Zhang, Z.H. Liu, Q.Z. Cai, J.H. Liu, C.K. Chua, Influence of Ni content on microstructure of W-Ni alloy produced by selective laser melting, Int. J. Refract. Met. H. 45 (2014) 15–22.
[19] S.H. Sun, Y. Koizumi, S. Kurosu, Y.P. Li, H. Matsumoto, A. Chiba, Build direction dependence of microstructure and high-temperature tensile property of Co–Cr–Mo alloy fabricated by electron beam melting, Acta Mater. 64 (2014) 154–168.
[20] S.H. Sun, Y. Koizumi, S. Kurosu, Y.P. Li, A. Chiba, Phase and grain size inhomogeneity and their influences on creep behavior of Co–Cr–Mo alloy additive manufactured by electron beam melting, Acta Mater. 86 (2015) 305–318.
[21] L. Thijs, F. Verhaeghe, T. Craeghs, J. Van Humbeeck, J.P. Kruth, A study of the microstructural evolution during selective laser melting of Ti–6Al–4V, Acta Mater. 58 (2010) 3303–3312.
[22] S.S. Al-bermani, M.L. Blackmore, W. Zhang, I. Todd, The origin of microstructural diversity, texture, and mechanical properties in electron beam melted Ti-6Al-4V, Metall. Mater. Trans. A 41A (2010) 3422–3434.
[23] A.A. Antonysamy, J. Meyer, P.B. Prangnell, Effect of build geometry on the β-grain structure and texture in additive manufacture of Ti6Al4V by selective electron beam melting, Mater. Charact. 84 (2013) 153–168.
[24] B. Vrancken, L. Thijs, J.P. Kruth, J. Van Humbeeck, Microstructure and mechanical properties of a novel β titanium metallic composite by selective laser melting, Acta Mater. 68 (2014) 150–158.
[25] T. Ishimoto, K. Hagihara, K. Hisamoto, S.H. Sun, T. Nakano, Crystallographic texture control of beta-type Ti–15Mo–5Zr–3Al alloy by selective laser melting for the development of novel implants with a biocompatible low Young's modulus, Scr. Mater. 132 (2017) 34–38.
[26] Z.H. Liu, D.Q. Zhang, C.K. Chua, K.F. Leong, Crystal structure analysis of M2 high speed steel produced by selective laser melting, Mater. Charact. 84 (2013) 72–80.
[27] Z.H. Liu, D.Q. Zhang, S.L. Sing, C.K. Chua, Interfacial characterisation of SLM parts in multi material processing: metallurgical diffusion between 316L stainless steel and C18400 copper alloy, Mater. Charact. 94 (2014) 116–125.
[28] L.E. Loh, C.K. Chua, W.Y. Yeong, J. Song, M. Mapar, S.L. Sing, Z.H. Liu, D.Q. Zhang, Numerical investigation and an effective modelling on the selective laser melting (SLM) process with aluminium alloy 6061, Int. J. Heat Mass Transf. 80 (2015) 288–300.
[29] L.P. Lam, D.Q. Zhang, Z.H. Liu, C.K. Chua, Phase analysis and microstructure characterisation of AlSi10Mg parts produced by selective laser melting, Virtual Phys. Prototyp. 10 (2015) 207–215.
[30] G. Van Tendeloo, Short range order considerations and development of long range order in different Ni-Mo alloys, Mater. Sci. Eng. 26 (1976) 209–220.
[31] L.A. Nesbit, D.E. Laughlin, Ordering in an off-stoichiometric Ni-Mo alloy, Acta Metall. 26 (1978) 815–825.
[32] S. Hata, S. Matsumura, N. Kuwano, K. Oki, Short range order and its transformation to long range order in Ni_4Mo, Acta Metall. 46 (1998) 881–892.
[33] S. Hata, T. Mitate, N. Kuwano, S. Matsumura, D. Shindo, K. Oki, Short range order structures in fcc-based Ni-Mo studied by high resolution transmission electron microscopy with image processing, Mater. Sci. Eng. A 312 (2001) 160–167.
[34] A. Hellawell, P.M. Herbert, The development of preferred orientations during the freezing of metals and alloys, Proc. Royal Soc. A 269 (1962) 560–573.